J. Fluid Mech. (1970), *vol.* 44, *part* 1, *pp.* 33–49
Printed in Great Britain

Cavity surface wave patterns and general appearance

By CHRISTOPHER BRENNEN
California Institute of Technology Pasadena, California

(Received 19 August 1968 and in revised form 9 January 1970)

Observations were made of the appearance of hydrodynamic cavities behind a series of axisymmetric headforms. Among the phenomena investigated was the transition of the interfacial or separated boundary layer on the cavity surface. The first stage of this process, namely the spatial growth of instability waves could be distinguished by means of high-speed photography. Comparison is made with a theoretical instability analysis.

1. Introduction

The surface appearance of a fully developed cavity, or more specifically, the nature of the separated interfacial boundary layer, can have important side effects. The rate of diffusion of dissolved gas and/or heat into the cavity will be much greater when the interfacial layer becomes turbulent; this, in turn, may lead to increased cavity pressures (Brennen 1969*b*). Thus a qualitative study was made of the surface of cavities behind a series of axisymmetric headforms and the results of these experiments are discussed in the first part of this paper. When transition occurs on the cavity surface, the first stage of that process, namely growth of a select frequency instability produces a pattern of surface waves which are clearly visible in the high-speed photographs. In the latter part of this paper these wave patterns are studied in some detail and comparison is made with a theoretical, linear stability analysis of the separated boundary layer.

The experiments, which were carried out in the no. 2 water tunnel of Ship Division, N.P.L., employed various rotationally symmetric shapes of headform supported on the axis of the tunnel by a sting and strut system described in earlier papers (Brennen 1969*a*, *b*). Although the investigation was limited to axisymmetric bodies, some of the findings are expected to be qualitatively applicable to other types of fully cavitating flow.

Still photographs were taken with equipment giving a flash of some 10 → 30 μsec duration; thus the fluid motions were 'frozen' even at the highest tunnel velocity ($\sim$ 50 ft./sec). The experimental arrangement included provision for ventilating the cavities with measured flow rates of air and for measuring the cavity pressure as described in the earlier papers cited above. The normal tunnel equipment was used for measurement of tunnel pressure, velocity and temperature. The cavitation number and other data relevant to each photograph could thus be computed. Five different headforms were employed: (*a*) a 3 in. diameter sphere (figures 1 (*b*) and (*c*), plate 1); (*b*) a 3 in. diameter sphere cut off along a plane through the latitudinal line 68 degrees from the theoretical front stagnation point (referred to as the 'cut-away' sphere) (figures 1(*e*) and (*f*), plate 1); (*c*) a $1\frac{1}{8}$ in. diameter hemispherical head placed on the end of the sting which was of the same diameter (figure 2(*a*), plate 2); (*d*) an ogival-shaped head of axial length $3\frac{1}{2}$ in. and base diameter 2·34 in. (figures 1(*a*) and (*d*), plate 1), whose shape corresponded to that of a theoretical semi-infinite 'body' created by a particular axial source distribution; thus an approximate wetted surface pressure distribution could be calculated; (*e*) a 3 in. diameter disk set normal to the stream (figure 2(*b*), plate 2).

2. Surface appearance of cavities

For each of the five headforms photographs of both natural and ventilated cavities were taken at a series of tunnel velocities, U_T, the tunnel pressure taking roughly its lowest operational value in all cases. It was apparent not only in the photographs but also to the naked eye that the appearance of the cavity surface was markedly different depending on whether the cavity was or was not filled with the turbulent froth of bubbles and water associated with the re-entrant jet. Clearly there were intermediate states of incomplete filling; however, it should suffice to describe the completely filled and the 'fully developed' cases.

Figures 1(*a*) and (*b*), plate 1 represent examples of the former type, referred to as being partially developed and confined almost exclusively to the natural cavity flows. Ventilation seemed to produce either a train of bubbles from the exit holes or a fully developed cavity flow (as defined below) with virtually no intermediate state. The following observations seemed generally applicable to the 'filled' cavities: (i) The ogive and the cut-away sphere (both of which have a sharp, separating edge) produced 'filled' cavities typified by figure 1(*a*). The characteristic gap of clear water between the base of the headform and the cavity is a somewhat surprising feature. In other photographs the gap may not have extended right to the centre of the base but always appeared near its periphery. The irregularities of the surface of the cavity do seem on examination to contain a characteristic frequency or wavelength which may be associated with a vortex shedding frequency from the sharp trailing edge of the head form (these frequencies are considerably smaller than those discussed in the later part of the paper). (ii) Under the same conditions the two spheres, having no sharp 'separating' edge, produced partially developed cavities which were much less steady (figure 1(*b*) being a typical example) and could be adequately described as being in an advanced state of incipient cavitation.

A cavity was considered to be 'fully developed' when the region just behind the headform became a single gas/vapour filled space; that is when the re-entrant jet no longer penetrated forward to the back of the body. As the length of the cavity further increases the proportion of cavity filled by the jet clearly decreases. It was incidentally observed that the 'strength' and penetration of the jet within a natural cavity was noticeably greater than for a ventilated cavity under identical conditions of tunnel velocity and cavity length. This may be associated with the different mass rates of vapour and gas entrainment into the wake as discussed in an earlier paper (Brennen 1969*b*). Whenever the jet impinged on the cavity wall the latter became rough, unsteady and opaque as in the bottom left-hand corner of figure 1 (*c*).

Attention will now be focused exclusively on the nature of cavity surfaces which are unaffected by such interference. The singular appearance of the interface just downstream of separation was first noted in photographs of the 3 in. sphere, figure 1 (*c*) being a typical example. Immediately following separation the surface is smooth and glassy. Downstream of this waves with crests running perpendicular to the direction of flow grow on the clear surface until they break up to form the rough or turbulent surface which persists along the rest of the length of the cavity. The naked eye could detect the two regions of smooth and turbulent surface though not the intervening wave pattern. Also visible in the case of the 3 in. sphere were the longitudinal striations which, especially near separation tended to disturb the described pattern (see figure 1 (*c*)). These striations may have been caused by small drops of water (from condensation or the spray of the re-entrant jet) being trapped in the very thin cavity just after separation. The drops and associated striations continually moved downwards under the influence of gravity. No such thin cavity region occurs with the cutaway sphere or ogive and, as can be seen from figures 1 (*d*) and 1 (*e*), there are no striations. Similar, but fixed, striations can be caused by irregularities in the headform at or near separation (Gadd & Grant 1965).

3. Further observation of the wave patterns

The waves observed shortly after separation have been noticed by some previous experimenters (for example, Acosta & Hamaguchi 1967) though to the author's knowledge no particular investigation has previously been made of them. They represent the cavity flow equivalent of the instabilities in the free shear layer of a one-phase wake flow. Waugh & Stubstad (1956) observed somewhat similar wave patterns on the surface of water-entry cavities. However, their waves appear to have been caused by longitudinal vibration of the disk-faced missile immediately following impact; with further submergence the cavity produced is smooth and similar to that of figure 2 (*b*), plate 2.

The present investigation involved studies of the wave patterns through still photographs and movie films, the results being listed below.

Still photographs

For a particular headform the wavelength, λ, and the distance from separation to wave break up, X_1, appeared to be functions only of the 'potential free streamline velocity', $U_\infty = U_T(1+\sigma)^{\frac{1}{2}}$, both increasing as this velocity decreased ($\sigma = (p_T - p_c)/\frac{1}{2}\rho U^2$ is the cavitation number). Changing the tunnel or cavity pressure (p_T or p_c) only affected the pattern indirectly by altering σ. Since fully developed cavities are restricted to a limited range of σ (about $0 < \sigma < 0{\cdot}5$) the principal variation was with tunnel velocity, U_T.

Further tests showed that ventilating the cavities had no observable effect upon the wave pattern beyond the change in U_∞. Thus the phenomenon could be studied at tunnel speeds down to about 10 ft./sec where it was not possible to create fully developed natural cavities.

With the 3 in. and cutaway spheres wave break up ceased to occur when the tunnel speed was reduced below about 14 ft./sec and the waves persisted along the length of the cavity (figure 1 (*f*)). In the case of the 1⅛ in. sphere the critical speed was about 17 ft./sec (see figure 2 (*a*)) though for this headform the wave patterns were not so remarkably regular as in the cases of the larger spheres. This may have been due to surface disturbances caused by the ventilation air which is emitted radially rather than in the downstream axial direction of the other headforms. With the ogive, transition occurred at all tunnel speeds (figure 1 (*d*)). However, the last headform, the 3 in. disk, produced completely clear cavities (as in figure 2 (*b*)) under all conditions. Some tests were carried out to determine whether by artificially increasing the noise level in the attached boundary layer an instability could be excited. Figures 2 (*c*) and (*d*) were the results of two crude attempts to do this; the results are clearly inconclusive since frequencies of vortex shedding from the disturbers (a row of pegs in figure 2 (*c*), a square-sectioned ring in figure 2 (*d*)) may be reflected in the free surface.

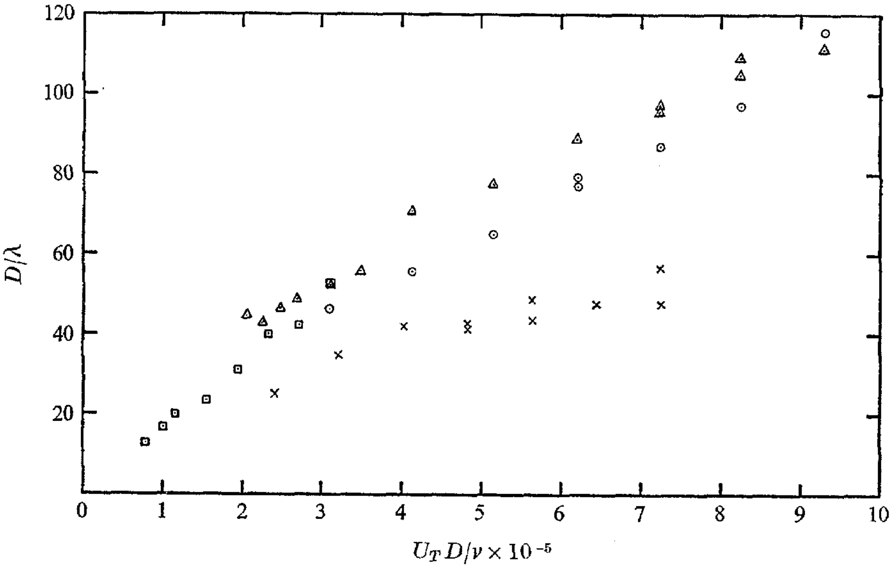

FIGURE 3. Variation of measured wavelengths, λ, with tunnel velocity, U_T: $\odot$, 3 in. sphere; $\triangle$, cutaway sphere; $\boxdot$, 1⅛ in. sphere; $\times$, ogive.

From each photograph measurements were made of λ and X_1. The distance from separation to the point at which λ was measured was also recorded. The X_1 measurement was somewhat arbitrary, especially for the ogive cavities. However, in most cases, a study of the profile of the cavity indicated a fairly distinct wave break-up point. In figures 3 and 4, λ and X_1 are plotted non-dimensionally against a Reynolds number, $U_T D/\nu$ (D being the diameter of the sphere or of the base of the ogive).

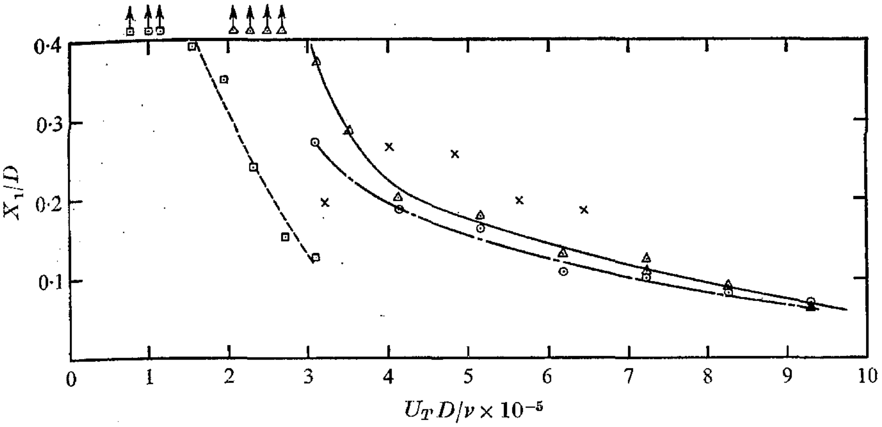

FIGURE 4. Variation of measured distance to wave break up, X_1, with tunnel velocity, U_T: -—⊙—-, 3 in. sphere; —△—, cutaway sphere; --□--, $1\frac{1}{8}$ in. sphere; ×, ogive. Speeds for which virtually no break up occurred are marked with the arrows.

Movie photography

It was clearly of interest to attempt to measure the propagation velocities of the waves by taking high-speed movie films of the flow. Using a Fastax camera the filming speed was limited to a maximum of about 4000 frames/sec because of the difficulty in beaming enough light on the subject through large Perspex windows and 2 ft. of water. This filming speed, in turn, set an upper limit on the tunnel velocity (about 20 ft./sec) for which the movement of individual waves between successive frames could be satisfactorily discerned. However for flow conditions similar to those of figures 1 (*e*) and (*f*), wave velocities could be estimated from a study of about 12 successive frames. Within the order of accuracy of measurement (about 5 %) no difference could be distinguished between the wave velocity and the potential free surface velocity, U_∞. This is not surprising in the light of the following simple calculation. Under the influence of surface tension, S, and a centripetal acceleration given by $U_T^2(1+\sigma)/R^*$ where R^* is the longitudinal curvature of the interface, a dynamic wave would have a velocity relative to the fluid motion of

$$\left[\frac{2\pi}{\lambda}\frac{S}{\rho}+\frac{U_T^2(1+\sigma)}{R^*}\frac{\lambda}{2\pi}\right]^{\frac{1}{2}}. \tag{1}$$

In the case, for example, of the cutaway sphere the first and second terms within the bracket would be of the order of 0·002 and 0·1 ft.^{2}/sec^2 respectively and the relative wave velocity would be small.

4. Stability analysis of the separated boundary layer

Stability analysis of the separated boundary layer is considerably simplified by using the planar flow model of figure 5. The model is expected to be fairly accurate since (1) both the distance of the separation point from the axis and the longitudinal radius of curvature are large compared with the boundary-layer thickness and (2) the free surface is not far from parallel with the axis (except in the case of the disk). Then assuming constant cavity pressure and that the vapour/gas exerts a negligible shear stress, the conditions at the interface are those of constant normal and zero tangential stress. In addition, the momentum thickness is assumed to remain unaltered after separation. The mean flow is therefore similar to that in the wake of a thin flat plate (Sato & Kuriki 1961).

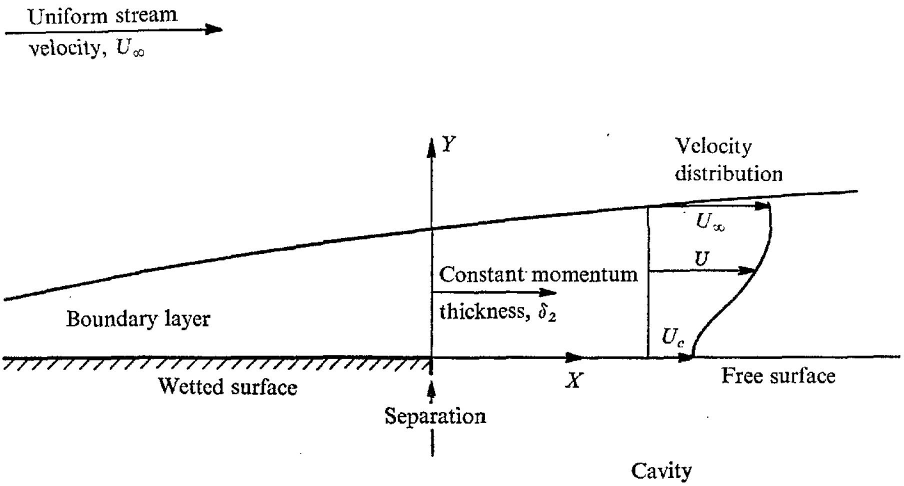

FIGURE 5. Mathematical model of boundary-layer flow at and following separation.

Non-dimensional co-ordinates are defined as $x = X/\delta_2$, $y = Y/\delta_2$ and $t = U_\infty T/\delta_2$ (T being time); the ratios of the velocities in the X, Y directions to U_∞ and of the pressure to ρU_∞^2 are denoted by u^*, v^* and p^* respectively. Following conventional linearized procedure and assumptions (see, for example, Betchov & Criminale 1967) the flow is split into mean and perturbation components

$$\left.\begin{aligned} u^*(x,y,t) &= u(x,y) + u_1(y)\,e^{i\alpha(x-ct)}, \\ v^*(x,y,t) &= \qquad\qquad v_1(y)\,e^{i\alpha(x-ct)}, \\ p^*(x,y,t) &= p(y) \quad + p_1(y)\,e^{i\alpha(x-ct)} \end{aligned}\right\} \tag{2}$$

and the equation of the interface is taken as

$$y = \xi^* = \xi_1 e^{i\alpha(x-ct)}. \tag{3}$$

In general both eigenvalues, α and c, are complex. Due to the constant cavity pressure, the mean flow pressure, p, is independent of x. However, a possible dependence upon y is included for later use. The equations governing the perturbations then become

$$i\alpha u_1 + \partial v_1/\partial y = 0, \tag{4}$$

$$i\alpha u_1(u-c) + v_1\frac{\partial u}{\partial y} + i\alpha p_1 = \frac{1}{R_{\delta_2}}\left(\frac{\partial^2 u_1}{\partial y^2} - \alpha^2 u_1\right), \tag{5}$$

$$i\alpha v_1(u-c) + \frac{\partial p_1}{\partial y} = \frac{1}{R_{\delta_2}}\left(\frac{\partial^2 v_1}{\partial y^2} - \alpha^2 v_1\right), \tag{6}$$

where R_{δ_2} is the Reynolds number based on momentum thickness, $U_\infty \delta_2/\nu$. The Orr–Sommerfeld eigenequation is obtained by eliminating p_1 and u_1 from these equations. Since the mean velocity distribution, u, changes with x and, presumably, with R_{δ_2} a complete solution would involve a knowledge of these distributions and the computation and tabulation of, say, α as a function of c for every x position for the required values of R_{δ_2}. Only the inviscid solution has been attempted here. Moreover, the mean velocity distribution has been approximated by the Gaussian form

$$w/w_c = e^{-\ln 2.(y/b)^2}, \tag{7}$$

where $w = 1-u$, $w_c(x) = 1-(u)_{y=0}$ and $b(x)$ is the half-width of the boundary layer (i.e. $w = \frac{1}{2}w_c$ at $y = b$). This satisfies the boundary condition of zero shear stress since $(\partial u/\partial y)_{y=0} = 0$ and has been chosen because of its apparent accuracy in the analogous thin plate wake flow (Sato & Kuriki 1961). However, it is expected to be least accurate close to separation (Goldstein 1933, Hollingdale 1940). The function $w_c(x)$ can, for the moment, remain unspecified and w_c used as a modified x co-ordinate, equal to unity at separation and tending to zero far downstream. It follows from the definition of δ_2 that

$$\frac{1}{b} = \left[\frac{\pi}{4\ln 2}\right]^{\frac{1}{2}} \left[w_c - \frac{w_c^2}{2^{\frac{1}{2}}}\right]. \tag{8}$$

Now the inviscid Orr–Sommerfeld equation can be written in the form

$$\left(\frac{w}{w_c} - k\right)\left(\frac{d^2 v_1}{dz^2} - \eta^2 v_1\right) - v_1 \frac{d^2}{dz^2}\left(\frac{w}{w_c}\right) = 0, \tag{9}$$

$$z = y/b; \quad k = (1-c)/w_c; \quad \eta = \alpha b. \tag{10}$$

Since (w/w_c) and its second derivative are independent of x (or w_c), the eigenvalues k, η are more general than the 'local' eigenvalues, α and c, at a particular x(or w_c).

The boundary conditions upon v_1 required for the eigensolution of (9) are as follows: (i) It is convenient to normalize $(v_1)_{y=z=0} = 1$. (ii) The linearized kinematic condition on $y = \xi^*$ gives

$$(v_1)_{y=z=0} = i\alpha\xi_1[(u_1)_{y=0} - c]. \tag{11}$$

(iii) The effect of surface tension, S, and of the centripetal acceleration due to longitudinal radius of curvature of the free surface in the actual flow (denoted by R^*) are included to yield a more general dynamic condition on $y = \xi^*$. It is assumed that R^* gives rise to a pressure gradient $\partial p/\partial y = u^2(\delta_2/R^*)$ in the mean flow. Gravitational acceleration is neglected since typical values of the centripetal acceleration far exceed it. The dynamic condition is then written as

$$p_c + \left[\frac{S}{\rho\delta_2 U_\infty^2}\frac{\partial^2 \xi^*}{\partial x^2}\right]_{y=\xi^*} \approx \left[p_c + \frac{\partial p}{\partial y}dy\right]_{y-dy=\xi^*} + (p_1)_{y=\xi^*}, \tag{12}$$

where p_c is the cavity pressure. With the conventional linear assumptions this becomes

$$(p_1)_{y=0} = -\xi_1\left[\alpha^2 \frac{S}{\rho\delta_2 U_\infty^2} + (1-w_c)^2 \frac{\delta_2}{R^*}\right]. \tag{13}$$

Substituting for ξ_1 from (11) and for $(p_1)_{y=0}$ from the inviscid form of (5) using $(\partial u/\partial y)_{y=0} = 0$ the boundary condition to be used in the eigensolution is

$$\frac{1}{(v_1)_{z=0}}\left(\frac{dv_1}{dz}\right)_{z=0} = -\frac{b}{w_c(1-k)}\left[\frac{\eta^2}{b^2}\frac{S}{\rho\delta_2 U_\infty^2}+\frac{\delta^2}{R^*}(1-w_c)^2\right] \tag{14}$$

$$= \Gamma = \Gamma_r + i\Gamma_i, \quad \text{say.}$$

This relates the real and imaginary parts of $(dv_1/dz)_{z=0}$ to the parameters $S/\rho\delta_2 U_\infty^2$ and δ_2/R^*. (iv) The usual outer boundary condition (Rosenhead 1966) was employed

$$\lim_{z\to\infty}\left[\frac{\partial v_1}{\partial z}+\eta v_1\right] = 0.$$

A computer program was written to calculate one of the eigenvalues η or k given the other and Γ. With an initial, guessed value of the unknown eigenvalue integrations were performed by the Runge–Kutta method starting at $z = 0$. Having obtained a value of $(\partial v_1/\partial z + \eta v_1)$ at large z the estimate was improved and the process repeated until the outer boundary condition was obeyed. The integrations were performed along a contour in a complex plane of z, chosen so as to avoid the singular point at $z^2 = -\ln k/\ln 2$.

5. Theoretical results

First an extensive series of eigenvalues were obtained for the case in which the effects of surface tension and curvature are neglected (i.e. $\Gamma = 0$). The results are plotted in figure 6 (the subscripts r and i refer to real and imaginary parts) and show a form very similar to those obtained by Betchov & Criminale (1967) in a analogous problem. The singularity around $k = 0{\cdot}24 - 0{\cdot}17i$ is clearly of the type discussed by those authors.

In the flow under investigation the disturbances are assumed to be growing only in space and not in time. Thus the real and imaginary parts of $\alpha . c$ must be equal to the non-dimensional frequency, γ, and zero respectively. It follows from the relations (10) that

$$\gamma = 2\pi f\frac{\delta_2}{U_\infty} = \frac{1}{b}[\eta_r - w_c(\eta_r k_r - \eta_i k_i)] \tag{15}$$

and

$$w_c = \eta_i/(\eta_r k_i + \eta_i k_r), \tag{16}$$

f being the frequency of the disturbance in the actual flow. Thus each point of figure 6 corresponds to purely spatial growth or decay for the frequency, γ, and at the 'x position' given respectively by (15) and (16). The spatial rate of amplification is given by $(1/A)\,dA/dx = -\eta_i/b$ where A is the general amplitude of ξ^*, u_1, v_1 or p_1. Replotting the results of figure 6, figure 7 shows how a disturbance of a given frequency, γ, is amplified ($\eta_i = -$ve) or suppressed ($\eta_i = +$ve) as it moves from separation ($w_c = 1$) to far downstream ($w_c \to 0$). Three points concerning the transformation from the k plane to the (w_c, γ) plane require further comment: (i) The neutral stability point in figure 6 ($\eta = 1{\cdot}598$, $k = 0{\cdot}6066$) transforms into the line $\gamma = 1{\cdot}598\,(1 - 0{\cdot}6066\,w_c)/b$. (ii) The line of maximum amplification is given by the locus of points for which $(\partial\eta_i/\partial w_c) = 0$. (iii) The mapping produces a singular point around $\gamma = 1{\cdot}76$, $w_c = 0{\cdot}95$. For values of η_i less than about $-0{\cdot}7$ the lower branch of the curve turns upward to produce a doubly-covered region as indicated by the dashed line for $\eta_i = -0{\cdot}8$. Physically this second sheet relates to disturbances of long wavelength (small η_r) and wave velocity greater than (and usually very much greater than) U_∞. For the moment the presence of this second sheet is disregarded; further comment is made below.

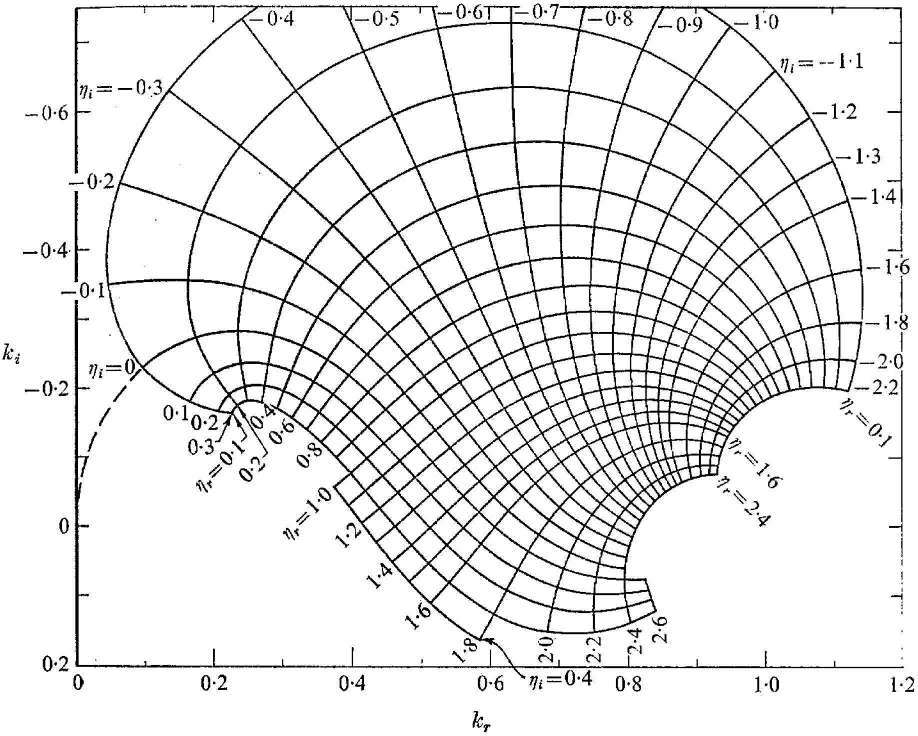

FIGURE 6. Eigenvalues k, η for the case $\Gamma = 0$.

If the noise in the boundary layer at separation was white (i.e. $(\partial A/\partial\gamma)_{w_c=1} = 0$) then it would appear from figure 7 that some frequency around 0·175 would receive maximum amplification over the distance $w_c = 1{\cdot}0$ to $0{\cdot}95$, say. The dominance of this 'preferred' frequency would increase with convection downstream since amplitude growth is exponential. Once the neutral point is reached (around $w_c = 0{\cdot}12$) no further amplification would take place. As illustrated by the experiments two possibilities arise: (1) sufficient amplification may occur before the neutral position for break up into turbulence to take place; otherwise (2) the waves will persist to very far downstream since damping is very small. The latter possibility may arise at the lower Reynolds numbers (see § 7).

Since finite amplification will take place over a finite distance it is instructive to integrate to find the total amplification at a particular position, w_c. For this purpose define ϕ as

$$\phi = \frac{1}{R_{\delta_2}} \ln\left(\frac{A}{A_s}\right) = \int_1^{w_c} -\frac{\eta_i}{b} \frac{d}{dw_c}\left(\frac{x}{R_{\delta_2}}\right) dw_c, \tag{17}$$

where A/A_s is the ratio of the amplitude at the point w_c to that of the noise at separation ($w_c = 1$). But to perform the integration, knowledge of the function $w_c(x)$ is needed. If Goldstein's (1933) formula for a flat plate laminar wake is used, i.e.

$$w_c = s^{\frac{1}{2}} + \tfrac{1}{2}s, \quad \text{where} \quad s = \frac{R_{\delta_2}}{\pi(x+x_0)}, \tag{18}$$

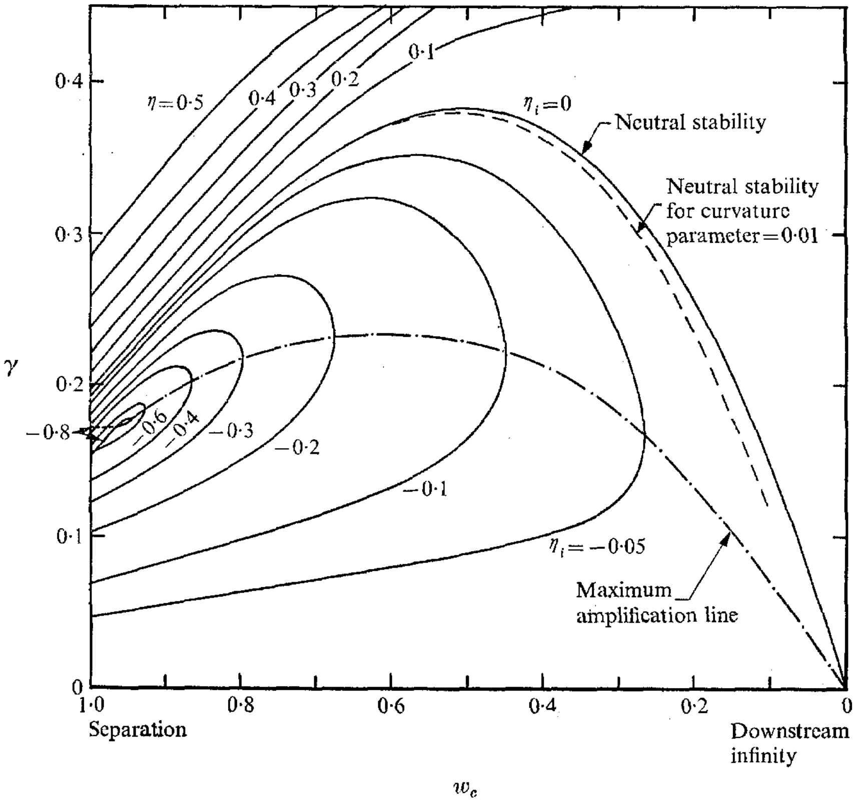

FIGURE 7. The stability results plotted in a graph of frequency, γ, and 'position', w_c.

integration leads to the results shown in figure 8. Again this suggests that provided $(\partial A_s/\partial\gamma)_{w_c=1} = 0$ the preferred frequency should be around 0·175; for $\gamma_c = 0·332$ the net amplification at the neutral point is zero. Discussion of nonlinear effects is postponed until the next section. Other possible influences examined were as follows: (i) Some eigensolutions were obtained with non-zero values of Γ in order to assess the effects of surface tension and curvature. Since the relation (14) contains the eigenvalues, computations were performed with chosen complex values of Γ, the corresponding magnitudes of the parameters

$S/\rho\delta_2 U_\infty^2$ and δ_2/R^* being post-calculated. In particular the effect upon the neutral stability line (figure 7) was studied; predictably finite and positive values of either or both parameters had a stabilizing effect, the values of γ at a particular w_c being lower than for the $\Gamma = 0$ case. But the effects of typical experimental values of $S/\rho\delta_2 U_\infty^2$ (maximum around 10^{-4}) were indistinguishable on the scale of figure 8. The influence of curvature, δ_2/R^*, was also small; the neutral stability line for $\delta_2/R^* = 0{\cdot}01$ is shown in figure 8, though experimentally this parameter is unlikely to have exceeded 5×10^{-4}. (ii) Two viscous effects upon the eigen-solution may be distinguished: (*a*) the inclusion of the viscous terms to produce

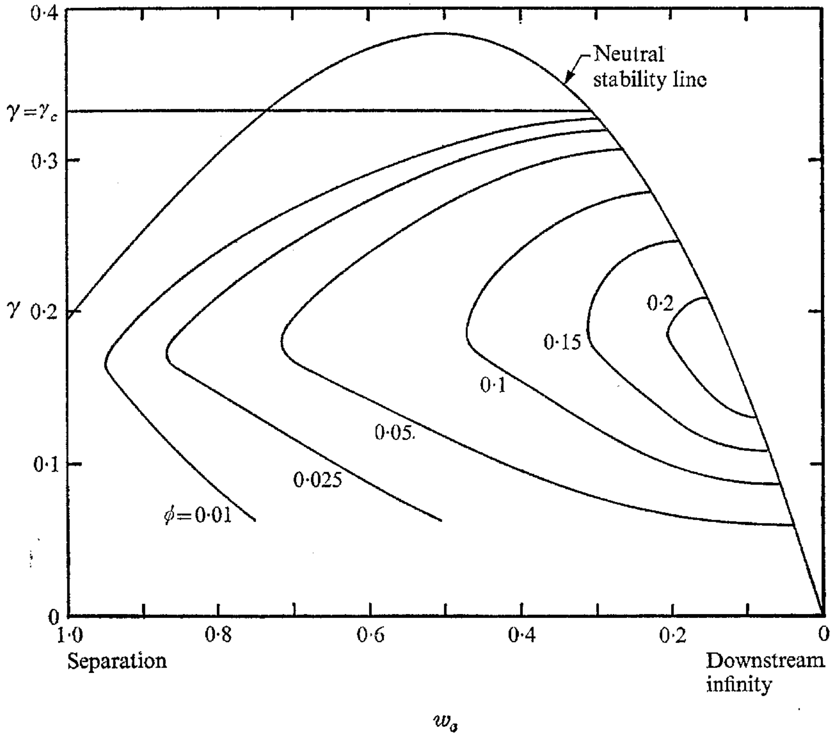

FIGURE 8. Integration of the linear stability characteristics yields $\phi = 1/R_{\delta_2} \ln (A/A_s)$ as a function of γ and w_c.

the full Orr–Sommerfeld equation and (*b*) the influence of Reynolds number on the velocity distribution, w/w_c. Since we are primarily concerned with the spatially-growing cases, the first effect is probably small. The results of McKoen (1955), Tatsumi & Kakutani (1958) and Kaplan (1964) demonstrate that in the analogous wake and jet flows this viscous effect is negligible above about $R_{\delta_2} = 150$. However the velocity distribution may be sufficiently far from Gaussian at or shortly after separation (e.g. Hollingdale 1940) for the second effect to be appreciable particularly at the lower Reynolds numbers. (iii) The spectral distribution of noise in the separating boundary layer (i.e. $A_s(\gamma)$) will have some effect in governing the preferred frequency. The discussion above was confined to disturbances relevant to the first sheet in figure 7; that is to say, to the treatment of noise having a propagation velocity less than U_∞ and therefore due to headform surface roughness, slight instability or irregularity in the attached boundary-layer flow, etc. The presence of the second sheet may provoke speculation as to how and under what conditions acoustic noise, for example, might become important.

6. Comparison of theory and experiment

In order to correlate the experimental results and compare them with theory, some estimate of the momentum thickness at separation, δ_2, was required for each of the axisymmetric headforms. The integral method of Rott & Crabtree (1952) was used in conjunction with theoretical wetted surface pressure distributions for the cavitating sphere and disk obtained previously (Brennen 1969*a*) and for the ogive obtained from the source distribution around which that headform was designed. The resulting values of $I = \delta_2/[D\nu/U_T]^{\frac{1}{2}}$ were 0·29, 0·061 and 0·746 for the sphere, disk and ogive respectively. But actual separation from the spheres took place some distance downstream of the position predicted by theory (Brennen 1969*a*). To make allowance for this the pressure distribution was extended by a constant pressure region to the actual separation position, as suggested by the experimental evidence (Brennen 1969*c*). The modified values of I were 0·30 for the cutaway sphere, 0·31 for the 3 in. sphere and 0·34 for the $1\frac{1}{8}$ in. sphere.

The results of figures 3 and 4 are replotted non-dimensionally in figures 9 and 11. But the wavelengths, λ, were measured at differing X/δ_2 positions and conversion to frequency was desirable for proper correlation; thus estimates of wave velocity were sought. For the limited number of cases studied through movie photography (see § 3) the non-dimensional wave velocity was close to unity. Unfortunately the flows for which break up occurs at relatively small X/δ_2 are those for which the velocity of the observable waves is likely to be significantly different from unity and at the same time those for which no satisfactory photographic measurement of wave velocity could be made (principally in the case of the ogival cavities). However, the calculations of the last section indicated that this velocity was relatively invariant with X/δ_2 in the range of X/δ_2 for which measurements of λ were made and that the wave velocities may be given roughly by $(1-0{\cdot}75\,\alpha_r)$. Using this, frequencies corresponding to results of figure 9 were plotted in figure 10.

Experimentally observed frequencies in the wake of a thin flat plate are also shown in figure 10. The results of Hollingdale (1940) and Taneda (1958) have been converted using $\delta_2 = 0{\cdot}664\,\nu L/U_\infty$. Sato & Kuriki's (1961) measurements being made at $w_c = 0{\cdot}692$, the conversion involved the relation (8).

Both types of flow indicate an inviscid frequency fairly close to the 0·175 suggested by the theory. The flat plate results seem to agree with the theoretical predictions of Tatsumi & Kakutani (1958) and Kaplan (1964) on two counts: (i) the preferred frequency does appear to be influenced by viscous effects below

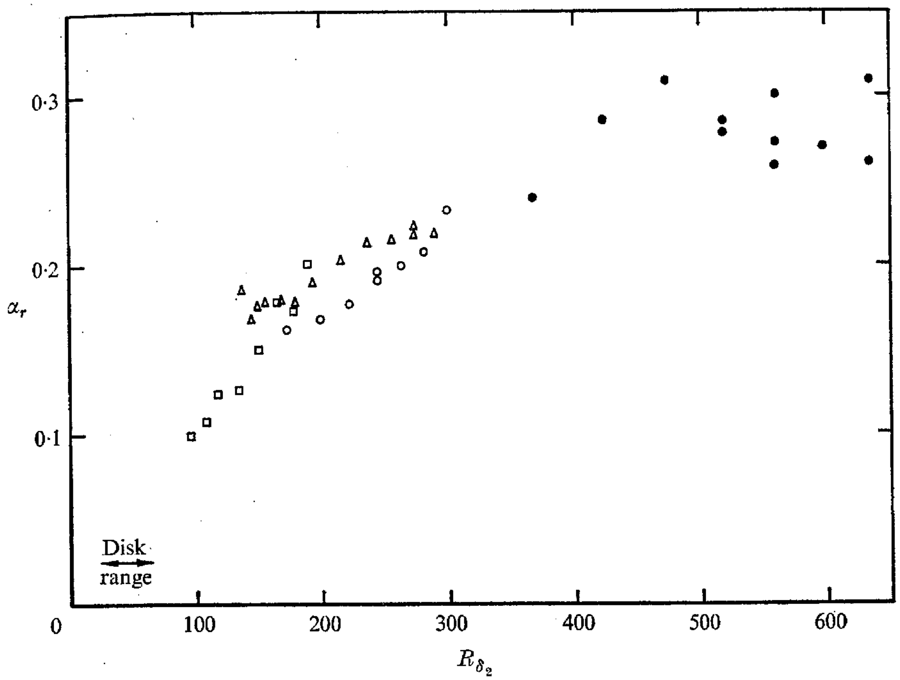

FIGURE 9. The results of figure 3 in dimensionless form; ⊙, 3 in. sphere; △, cutaway sphere; ⊡, $1\frac{1}{8}$ in. sphere; ●, ogive. The range of Reynolds number in which the disk operates is indicated by the arrows.

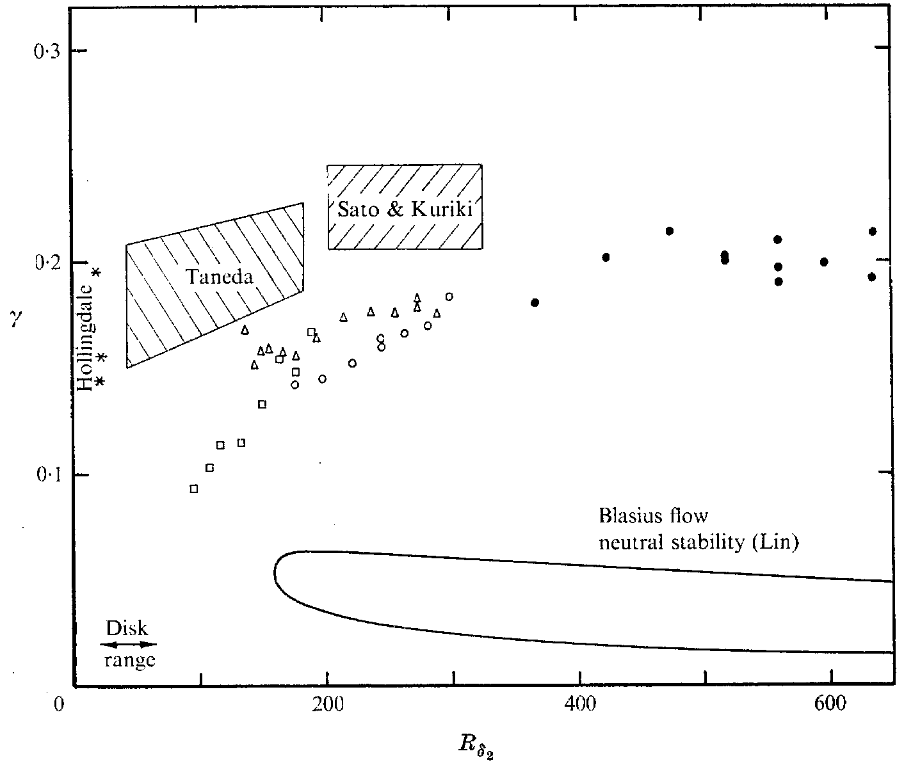

FIGURE 10. Non-dimensional instability frequencies plotted against R_{δ_2}; ⊙, 3 in. sphere; △, cutaway sphere; ⊡, $1\frac{1}{8}$ in. sphere; ●, ogive; ↔, range of disk operation. Also shown are the experimental results for the wake of a thin flat plate from Sato & Kuriki, Taneda and Hollingdale (*) and the neutral stability curve for Blasius boundary-layer flow (Lin).

about $R_{\delta_2} = 150$ and (ii) their critical R_{δ_2} of 4 is of the same order as that observed by Hollingdale and Taneda (~ 17).

The cavity surface results exhibit a somewhat greater dependence upon R_{δ_2} which may be due to a greater variation of velocity distribution with R_{δ_2} than in the case of the flat plate (see last section). The fact that no waves were observed on the disk cavities ($27 < R_{\delta_2} < 60$) suggests a critical R_{δ_2} of around 70. Some other experiments with small spherical headforms appeared to confirm this value (Brennen 1968). However, in the case of the disk, the greater axisymmetric divergence of the free surface following separation may also have had an effect, the momentum being dispersed over an increasing area as it is convected downstream.

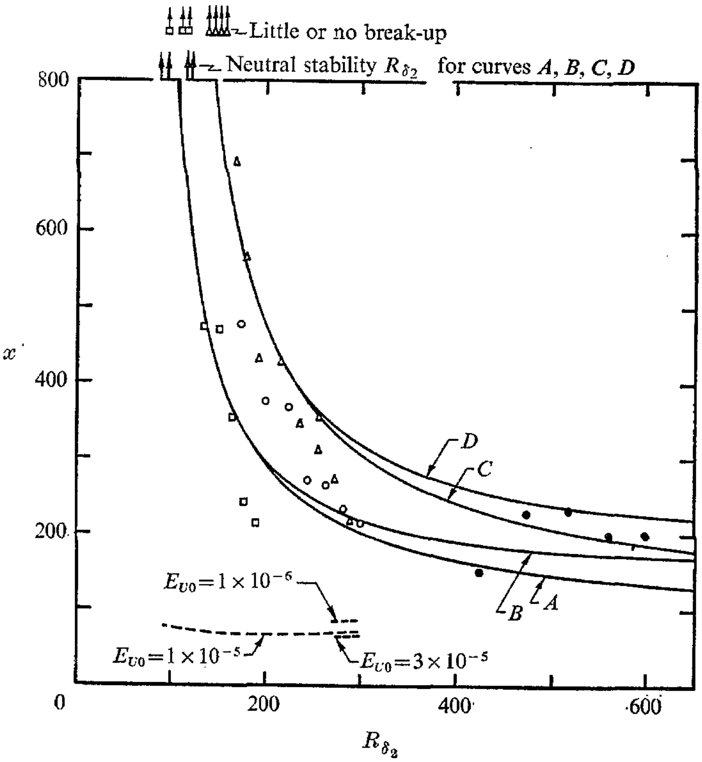

FIGURE 11. The results of figure 4 in dimensionless form: ⊙, 3 in. sphere; △, cutaway sphere; ⊡, $1\frac{1}{8}$ in. sphere; ●, ogive. Lines of constant total amplification, A/A_s, from linear theory:

Line	γ	$\ln(A/A_s)$	Neutral stability at R_{δ_2}	Neutral stability at x
A	0·18	20	89	2020
B	0·20	20	95	1669
C	0·18	25	111	2525
D	0·20	25	119	2085

The positions of fluctuation energy peaks in the non-linear flat plate wake theory of Ko, Kubota & Lees are shown (– – – –) for three different initial energies, E_{U0}.

7. Wave break up

The positions of wave break up are plotted in figure 11. In this respect there is considerable difference between the flat plate wake and cavity results. When R_{δ_2} is greater than 80, say, the fluctuations in a flat plate wake reach non-linear proportions at about $x = 70$, or, in other words at a distance of about 3 wavelengths from the trailing edge (see Taneda; Sato & Kuriki). It is clear from the photographs that in the cavity flows non-linear effects and wave break up do not occur until much further downstream. This is further illustrated by plotting in figure 11, the 'fluctuation energy peak' positions from the work of Ko, Kubota & Lees (1969). However the 'energy peak' position or the appearance of non-linear effects will be delayed by a reduction in the initial energy or noise level. It may be that in the present experiments the highly stable accelerating boundary layer on the wetted surface leads to a 'separating layer' which has a considerably lower noise level than that of the flat plate.

A study of the cavity profile indicated that the surface waves broke up when their amplitude reached a value of the same order as half a wavelength; this suggests that non-linear effects were only important in the last phase of the fluctuation growth. Integration of the linear stability results through equations (17) and (18) yielded the lines of constant total magnification which end at the neutral stability points shown in the table of figure 11. The points of wave break up lie predominantly in the band between A/A_s equal to e^{20} and e^{25}. Even taking into account the discussion of the last paragraph, total amplification of this order seems unrealistically high. The ratio of the typical amplitude at break up (half a wavelength $\approx 10^{-3}$ ft.) to the typical headform roughness ($\sim 0{\cdot}5 \times 10^{-6}$ ft.) is about e^8 (a figure very close to that quoted by Smith (1957) for the amplification up to the first appearance of turbulence in attached boundary layers). Non-linear effects will reduce the theoretical figures mentioned above; the results of Sato & Kuriki and Ko, Kubota & Lees indicate that the dx/dw_c term in the integral (17) can be as small as a third of the laminar-wake value in the non-linear region.

Despite their high A/A_s values, the lines A, B, C and D (figure 11) do appear to follow the experimental results in that their neutral stability Reynolds numbers are close to those for which break up ceased to occur.

8. Concluding remarks

One final observation may be of interest. The wave crests in figure 1 (*f*) become progressively more inclined to the vertical (or back face of the cutaway sphere) as they move downstream (see figure 12). Assuming uniform cavity pressure, the vertical gradient of the 'potential' cavity surface velocity (U_∞) should be $-g/U_\infty$, g being the gravitational acceleration. Since the wave propagation velocity in this case is little different from U_∞, the rate of increase in θ (figure 12) with X should be $d(\tan\theta)/dX = g/U_\infty^2$ which has a value of about 0·197 ft.$^{-1}$ for the conditions of figure 1 (*f*). This agrees satisfactorily with the slope (0·205 ft.$^{-1}$) of the line through measurements taken directly from figure 1 (*f*) (figure 12).

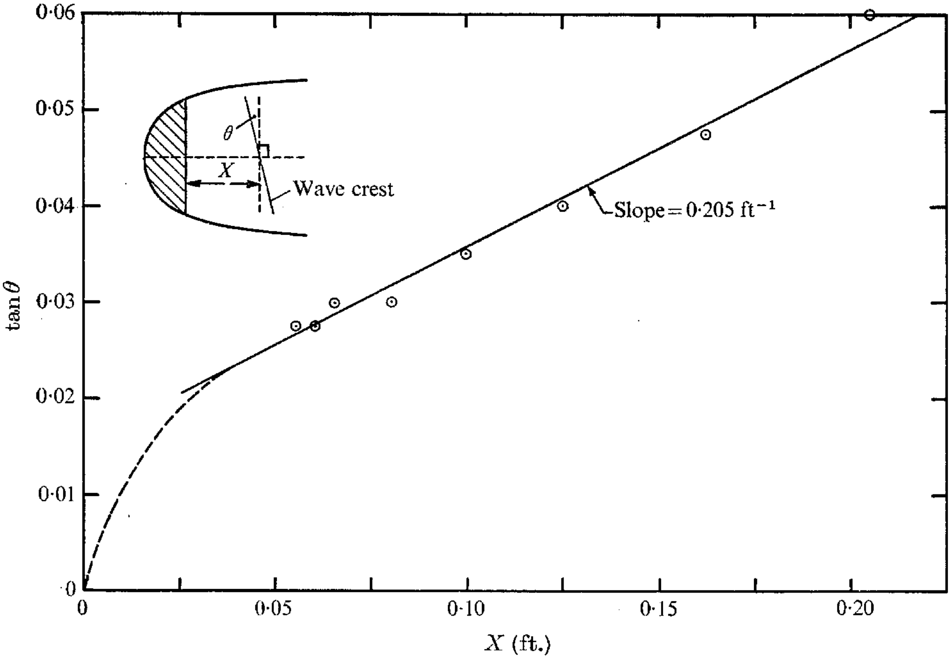

Figure 12. X variation of wave crest inclination to the vertical in figure 1 (f).

This work was carried out partly at the Ship Division, N.P.L. and partly under an O.N.R. Contract at the California Institute of Technology, Pasadena. The author wishes to thank Mr S. Grant (N.P.L.) for assistance with the experiments, Mr David Swindells (N.P.L.) for his expert photography and Dr G. E. Gadd, Dr A. Davey and Dr T. Y. Wu for valuable discussions on the subject.

REFERENCES

Acosta, A. J. & Hamaguchi, H. 1967 Cavitation inception on the ITTC Standard headform. *Cal. Inst. of Tech., Rep.* no. E-149, 1.

Betchov, R. & Criminale, W. O. 1967 *Stability of Parallel Flows*. Academic.

Brennen, C. 1968 Some cavitation experiments with dilute polymer solution. *N.P.L., Ship Division Rep.* no. 123.

Brennen, C. 1969*a* A numerical solution of axisymmetric cavity flows. *J. Fluid Mech.* **37**, 671.

Brennen, C. 1969*b* The dynamic balances of dissolved air and heat in natural cavity flows. *J. Fluid Mech.* **37**, 115.

Brennen, C. 1969*c* Some viscous and other real fluid effects in fully developed cavity flows. *Cavitation State of Knowledge, ASME.*

Gadd, G. E. & Grant, S. 1965 Some experiments on cavities behind disks. *J. Fluid Mech.* **23**, 4.

Goldstein, S. 1933 On the two-dimensional steady flow of a viscous fluid behind a solid body. *Proc. Roy. Soc.* A **142**, 545–562.

Hollingdale, S. H. 1940 Stability and configuration of the wakes produced by solid bodies moving through fluids. *Phil. Mag.* **7**, 29.

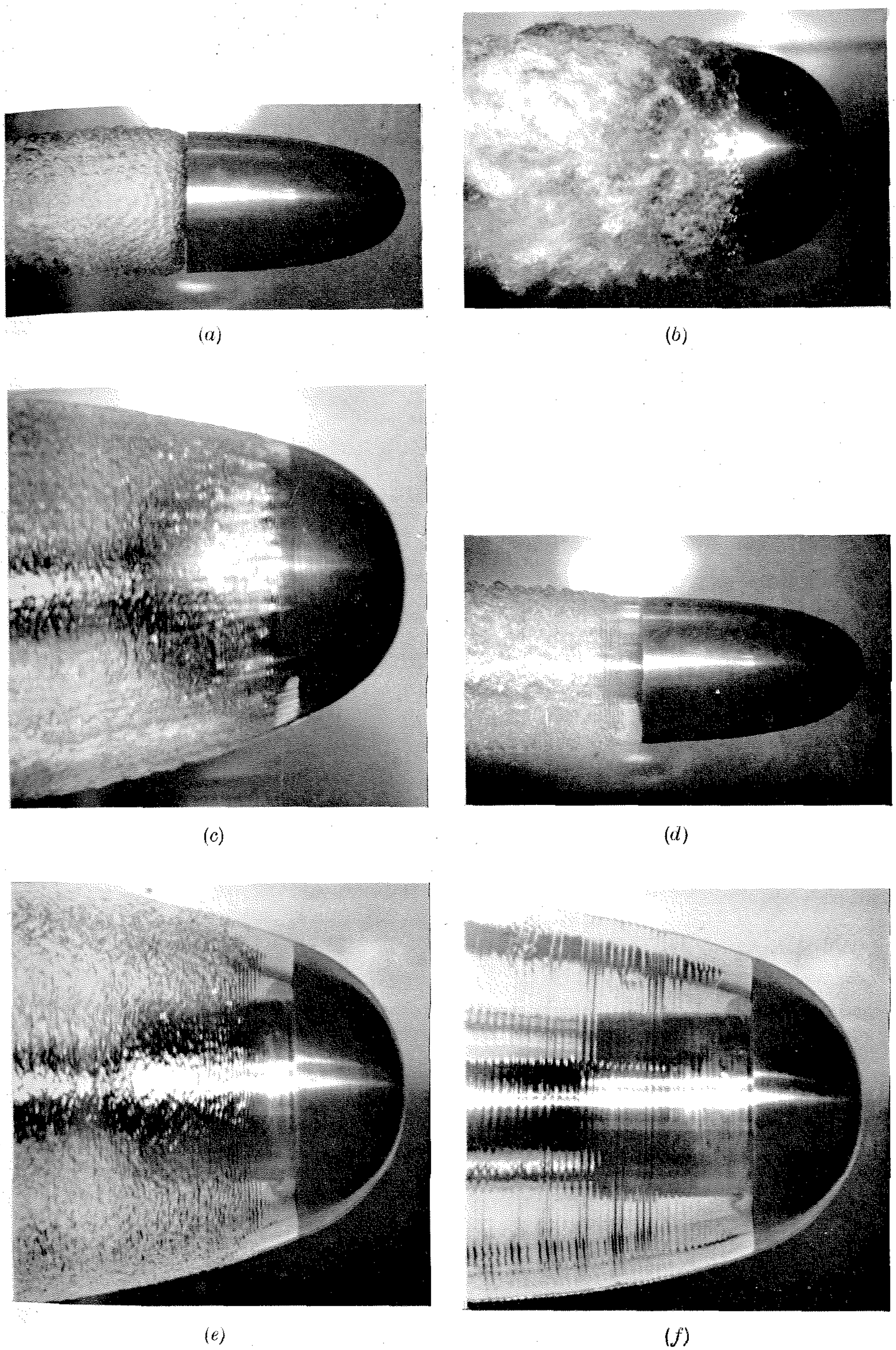

(*a*) (*b*) (*c*) (*d*) (*e*) (*f*)

FIGURE 1. (*a*) Ogive, $U_T = 30$ ft./sec, natural cavity. (*b*) 3 in. sphere, $U_T = 20$ ft./sec, natural cavity. (*c*) 3 in. sphere, $U_T = 35$ ft./sec, natural cavity. (*d*) Ogive, $U_T = 25$ ft./sec, ventilated cavity. (*e*) Cut-away sphere, $U_T = 20$ ft./sec, ventilated cavity. (*f*) Cut-away sphere, $U_T = 12$ ft./sec, ventilated cavity.

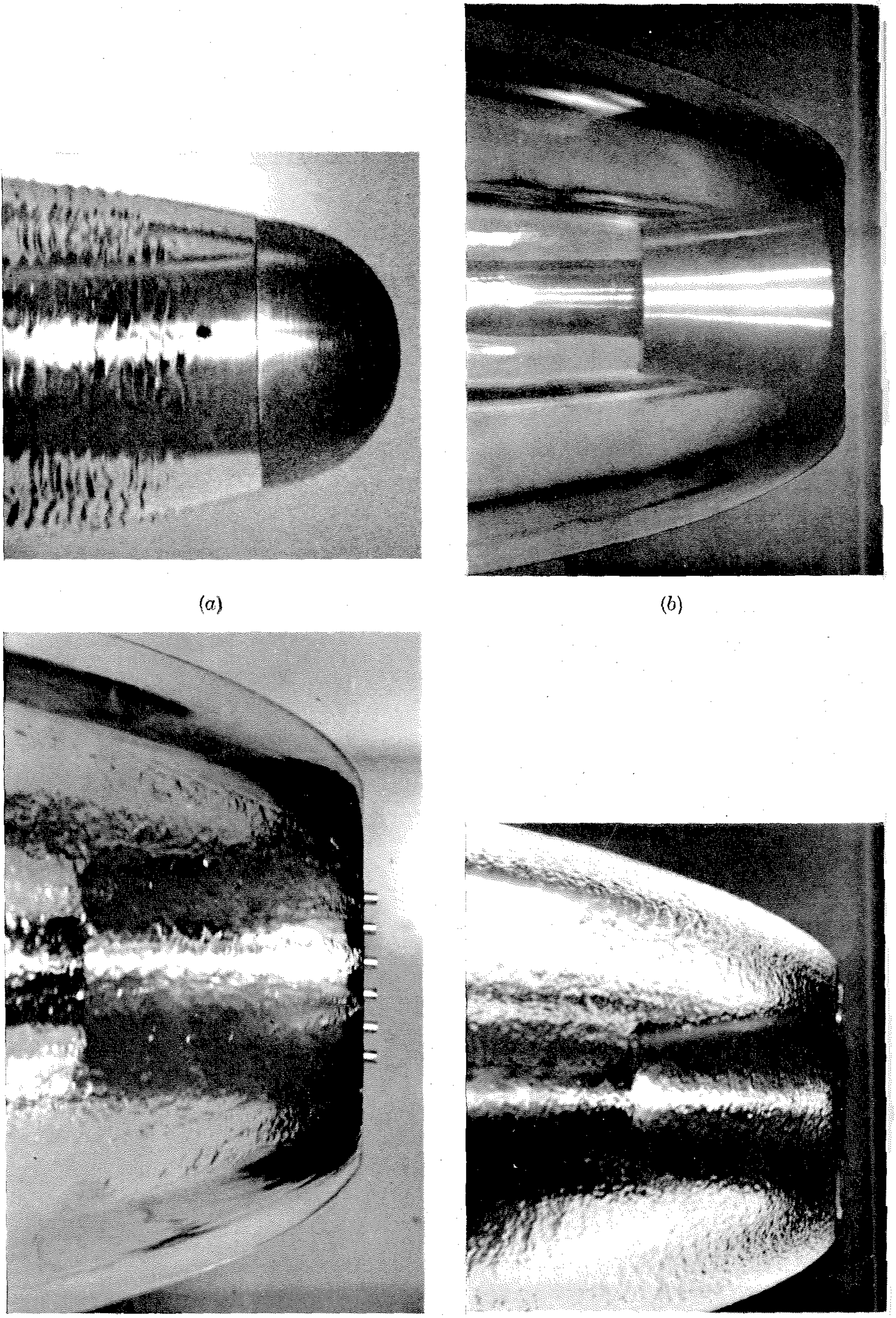

(*a*) (*b*)

(*c*) (*d*)

FIGURE 2. (*a*) $1\frac{1}{8}$ in. sphere, $U_T = 15$ ft./sec, ventilated cavity. (*b*) Disk, $U_T = 35$ ft./sec, ventilated cavity. (*c*) Disk with row of pegs on face, $U_T = 30$ ft./sec, ventilated cavity. (*d*) Disk with ring on face, $U_T = 30$ ft./sec, ventilated cavity.

KAPLAN, R. E. 1964 The stability of laminar incompressible boundary layers in the presence of compliant boundaries. *M.I.T., Aero-elastic and Structures Research Lab.*, ASRL-TR, 116-1.

KO, D. R. S., KUBOTA, T. & LEES, L. 1969 Finite disturbance effect on the stability of a laminar incompressible wake behind a flat plate. *Cal. Inst. of Tech., GALCIT Memo.* no. 72.

LIN, C. C. 1945 On the stability of two-dimensional parallel flows. *Quart. Appl. Math.* **3**, 117–42, 218–34, 277–301.

MCKOEN, C. H. 1955 Stability of laminar wakes. *Current Papers Aero. Res. Cam. Lond.* no. 303.

ROSENHEAD, L. 1966 *Laminar Boundary Layers.* Oxford University Press.

ROTT, N. & CRABTREE, L. F. 1952 Simplified laminar boundary layer calculations for bodies of revolution and for yawed wings. *J. Aero. Sci.* **19**, 553–65.

SATO, H. & KURIKI, K. 1961 The mechanism of transition in the wake of a thin flat plate placed parallel to a uniform flow. *J. Fluid Mech.* **11**, 321.

SMITH, A. M. O. 1957 Transition, pressure gradient and stability theory. *Proc. 9th Int. Cong. Appl. Mech.* **4**, 234–244.

TANEDA, S. 1958 Oscillation of the wake behind a flat plate parallel to the flow. *J. Phys. Soc. Japan*, **13**, 4.

TATSUMI, T. & KAKUTANI, T. 1958 The stability of a two-dimensional jet. *J. Fluid Mech.* **4**, 261.

WAUGH, J. G. & STUBSTAD, G. W. 1956 Water-entry cavity modelling. *NOTS* 1597, *NAVORD Report* 5365.